Astronomy & Astrophysics

Multifrequency polarimetry of high-synchrotron peaked blazars probes the shape of their jets

F. Bolis[1,2,★], E. Sobacchi[2,3], and F. Tavecchio[2]

[1] DiSAT, Università dell'Insubria, Via Valleggio 11, I-22100 Como, Italy
[2] INAF – Osservatorio Astronomico di Brera, Via E. Bianchi 46, I-23807 Merate, Italy
[3] Gran Sasso Science Institute, Viale F. Crispi 7, I-67100 L'Aquila, Italy

ABSTRACT

Multifrequency polarimetry is emerging as a powerful probe of blazar jets, especially with the advent of the Imaging X-ray Polarimetry Explorer (IXPE) space observatory. We studied the polarization of high-synchrotron peaked (HSP) blazars, for which both optical and X-ray emission can be attributed to synchrotron radiation from a population of nonthermal electrons. We adopted an axisymmetric stationary force-free jet model in which the electromagnetic fields are determined by the jet shape. When the jet is nearly parabolic, the X-ray polarization degree is $\Pi_X \sim 15$–50%, and the optical polarization degree is $\Pi_O \sim 5$–25%. The polarization degree is strongly chromatic: $\Pi_X/\Pi_O \sim 2$–9. This chromaticity is due to the softening of the electron distribution at high energies, and is much stronger than for a uniform magnetic field. The electric vector position angle (EVPA) is aligned with the projection of the jet axis on the plane of the sky. These results compare very well with multifrequency polarimetric observations of HSP blazars. When the jet is instead nearly cylindrical, the polarization degree is large and weakly chromatic (we find $\Pi_X \sim 70\%$ and $\Pi_O \sim 60\%$, close to the expected values for a uniform magnetic field). The EVPA is perpendicular to the projection of the jet axis on the plane of the sky. A cylindrical geometry is therefore practically ruled out by current observations. The polarization degree and the EVPA may be less sensitive to the specific particle acceleration process (e.g., magnetic reconnection or shocks) than previously thought.

Key words. acceleration of particles – magnetohydrodynamics (MHD) – galaxies: active – BL Lacertae objects: general – galaxies: magnetic fields – galaxies: nuclei

1. Introduction

Relativistic jets from supermassive black holes in active galactic nuclei (AGNs) shine through the entire electromagnetic spectrum, from the radio up to very high-energy gamma-rays (Romero et al. 2017; Blandford et al. 2019; Böttcher 2019). Nonthermal radiation carries a wealth of information on the dynamics, structure, and composition of AGN jets. Nonthermal radiation is best studied in blazars, a particular class of AGN where the jet is directed nearly along the line of sight, as the emission from the jet is strongly beamed due to the favorable orientation.

Multifrequency polarimetry is emerging as a powerful probe of blazar jets, especially with the advent of the Imaging X-ray Polarimetry Explorer (IXPE) space observatory (Liodakis et al. 2022; Di Gesu et al. 2022, 2023; Ehlert et al. 2023; Marshall et al. 2023; Middei et al. 2023a,b; Peirson et al. 2023; Errando et al. 2024; Kim et al. 2024). Here we focus on high-synchrotron peaked (HSP) blazars, for which both optical and X-ray emission can be attributed to synchrotron radiation from a population of nonthermal electrons. The observed X-ray polarization degree is $\Pi_X \sim 10$–20%, whereas the optical polarization degree is significantly smaller ($\Pi_X/\Pi_O \gtrsim 2$). The electric vector position angle (EVPA) seems to align with the projection of the jet axis on the plane of the sky. So far, IXPE has observed blazars in a quiescent state, when the polarization degree and the EVPA do not change significantly during the observing time (see however Di Gesu et al. 2023).

Multifrequency polarimetric observations of HSP blazars were interpreted as evidence that nonthermal electrons are accelerated in shocks (e.g., Liodakis et al. 2022). Several theoretical studies support this interpretation (for a review, see, e.g., Marscher & Jorstad 2021; Tavecchio 2021). However, it is far from evident that the shock acceleration scenario is the only way to interpret observations.

In this paper we study the polarization of the synchrotron radiation from Poynting-dominated jets, where particles are unlikely accelerated by shocks (Sironi et al. 2015). We show that the polarization degree and the EVPA are very sensitive to the jet shape, which determines the global structure of the electromagnetic fields (we neglect the presence of a random component of the fields that changes on small spatial scales). We find that multifrequency polarimetric observations of HSP blazars can be reproduced when the jet is nearly parabolic, whereas a cylindrical geometry is practically ruled out. The softening of the electron distribution at high energies is crucial to explaining the strong chromaticity of the polarization degree. In contrast with previous claims, we argue that current observations can hardly constrain the particle acceleration process.

The paper is organized as follows. In Sect. 2 we discuss the structure of the electromagnetic fields within the jet. In Sect. 3 we study the polarization of the synchrotron radiation. In Sect. 4 we discuss our results and conclude.

2. Jet structure

According to a widely accepted paradigm, relativistic jets extract the rotational energy of the supermassive black

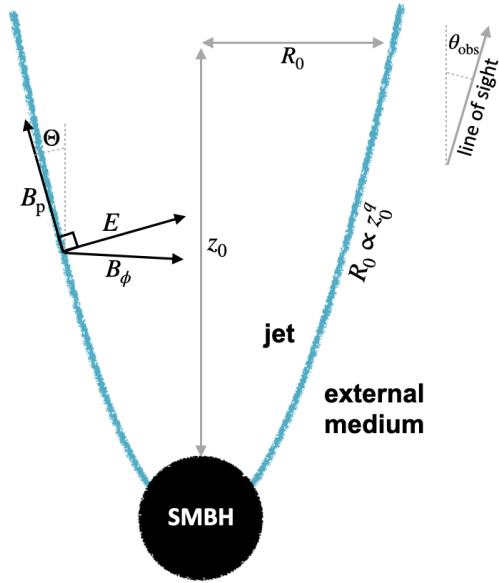★ Corresponding author; filippo.bolis@inaf.it

Fig. 1. Shape of the jet. The boundary radius, R_0, is proportional to z_0^q, where z_0 is the distance from the supermassive black hole. The value of the parameter $q < 1$ depends on the pressure profile of the external medium that collimates the jet. The line of sight makes an angle θ_{obs} with respect to the direction of the jet axis.

hole via electromagnetic stresses (Blandford & Znajek 1977; Blandford & Payne 1982; Tchekhovskoy et al. 2011). This process produces magnetized outflows, where most of the energy is carried in the form of Poynting flux. The structure of such Poynting-dominated outflows has been thoroughly investigated both numerically (Komissarov et al. 2007, 2009; Tchekhovskoy et al. 2008, 2009) and analytically (Vlahakis 2004; Lyubarsky 2009, 2010, 2011).

Lyubarsky (2009) derived the asymptotic equations that govern axisymmetric stationary outflows collimated by an external medium. These equations are valid far beyond the light cylinder, where the jet is accelerated to large Lorentz factors. The outflow is assumed to be force-free. The properties of the outflow are summarized below.

When the external pressure decreases as a power law, $\mathcal{P}_{ext} \propto z_0^{-\kappa}$, where z_0 is the distance from the black hole, the jet transverse radius can be parametrized as $R_0 \propto z_0^q$. For $0 < \kappa < 2$ one has $q = \kappa/4$, whereas for a wind-like medium with $\kappa = 2$ one has $1/2 < q < 1$ (when $\kappa = 2$, the value of q depends on the ratio of the magnetic and external pressure near the light cylinder). Very long baseline interferometry imaging of radio emission from AGNs jets suggests $q \sim 0.5$–1 (Mertens et al. 2016; Pushkarev et al. 2017; Kovalev et al. 2020; Boccardi et al. 2021). The shape of the jet is sketched in Fig. 1.

We adopted a cylindrical coordinate system (R, ϕ, z), where $\hat{\mathbf{z}}$ is directed along the jet axis. The electromagnetic fields can be presented as

$$\mathbf{E} = E_R\hat{\mathbf{R}} + E_z\hat{\mathbf{z}} \tag{1}$$

$$\mathbf{B} = B_R\hat{\mathbf{R}} + B_\phi\hat{\boldsymbol{\phi}} + B_z\hat{\mathbf{z}} , \tag{2}$$

where

$$E_R = \Omega R B_p \cos\Theta , \qquad E_z = -\Omega R B_p \sin\Theta \tag{3}$$
$$B_R = B_p \sin\Theta , \qquad B_z = B_p \cos\Theta . \tag{4}$$

The speed of light is set to $c = 1$. The angular velocity, Ω, and the poloidal magnetic field, B_p, are assumed to be independent of R. Numerical simulations show that this is a reasonable approximation (see, e.g., Fig. 4 of Komissarov et al. 2007).

The local jet opening angle, Θ, is determined by the shape of the magnetic flux surfaces. The boundary radius, R_0, can be parametrized as $\Omega R_0 = 3^{1/4} C(\Omega z_0)^q$, where C is a constant of order unity (Lyubarsky 2009). At the distance z_0 from the black hole, one has $\Theta \simeq |E_z/E_R| = qR/z_0$, which gives

$$\Theta = q \, \frac{R}{R_0} \, \frac{\left(3^{1/4}C\right)^{1/q}}{(\Omega R_0)^{(1-q)/q}} \, . \tag{5}$$

As we discuss in Appendix C, in the model of Lyubarsky (2009) the toroidal magnetic field is determined by

$$\frac{B_\phi^2 - E^2}{B_p^2} = \left(3^{1/4} \, C\right)^{2/q} \, \frac{q\,(1 - q)}{3} \, \frac{(\Omega R)^4}{(\Omega R_0)^{2/q}} \, . \tag{6}$$

Taking into account that $\Omega R_0 \gg 1$ far beyond the light cylinder, from Eqs. (3) and (6) one can show that $B_\phi \sim E_R \gg B_p$ in the observer's frame. However, the poloidal magnetic field cannot be neglected because the toroidal field and the electric field nearly cancel in the proper frame. The left panel of Fig. 2 shows the ratio of the toroidal and poloidal components of the magnetic field in the proper frame as a function of the distance from the jet axis. For small values of q (i.e., when the jet is nearly cylindrical) the poloidal component is larger than the toroidal component. For large q (i.e., when the jet opening angle increases) the toroidal component starts to dominate, especially near the jet boundary. As we explain in Sect. 3, these features are crucial for the polarization of the synchrotron radiation from the jet.

We assumed that the bulk velocity of the fluid, $\mathbf{v}$, is equal to the drift velocity, which is

$$\mathbf{v} = \frac{\mathbf{E} \times \mathbf{B}}{B^2} \, . \tag{7}$$

The right panel of Fig. 2 shows the corresponding Lorentz factor, $\Gamma = (1 - v^2)^{-1/2} = (1 - E^2/B^2)^{-1/2}$. The value of ΩR_0 is determined from the condition $\Gamma(R_0) = 10$, which is the typical Lorentz factor of AGN jets. For small values of q, the Lorentz factor increases linearly with the radius (i.e., $\Gamma \sim \Omega R$). For large values of q, the Lorentz factor peaks at intermediate radii. One can show that near the jet boundary the Lorentz factor is determined by the curvature of the magnetic flux surfaces. Small and large values of q correspond respectively to the first and second collimation regimes identified by Lyubarsky (2009).

3. Polarization

In order to study the polarization of the synchrotron radiation from the jet, we assumed that the energy distribution of the emitting electrons in the proper frame is

$$\frac{dN}{d\gamma} = K_e \gamma^{-p} \, , \tag{8}$$

where $K_e(R, z)$ is the proper electron number density. We also assumed that the distribution is isotropic.

The polarization of the synchrotron radiation from relativistic outflows has been investigated by several authors (e.g., Blandford & Königl 1979; Pariev et al. 2003; Lyutikov et al.
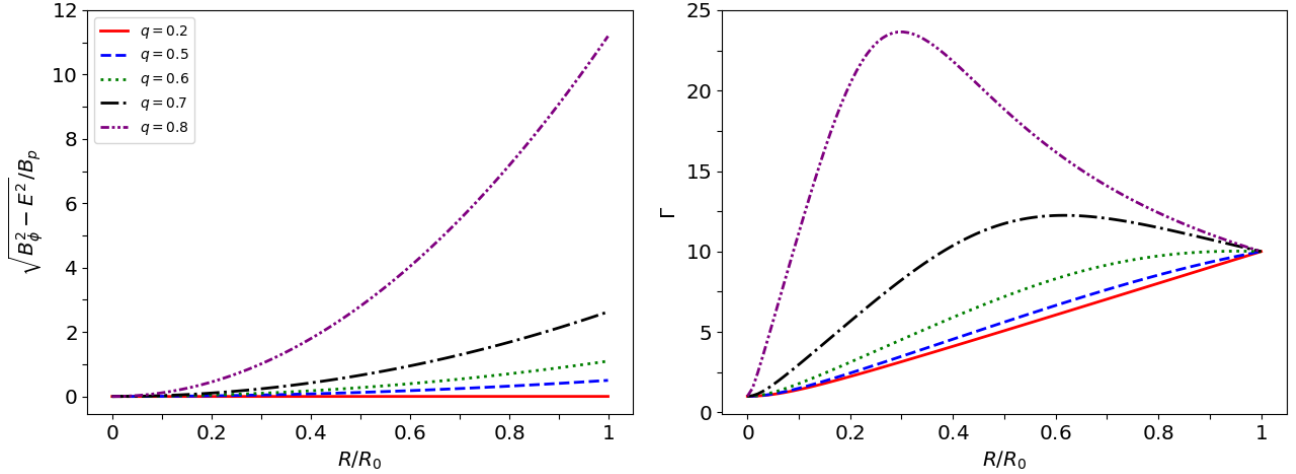
Fig. 2. Ratio of the toroidal and poloidal components of the magnetic field in the proper frame of the fluid (left panel) and bulk Lorentz factor of the fluid in the observer's frame (right panel) as a function of the distance, R, from the jet axis.

2003, 2005; Del Zanna et al. 2006). The Stokes parameters per unit length of a stationary jet are given by[1]

$$I = \frac{p + 7/3}{p + 1} \kappa_p \int dV K_e \mathcal{D}^{(3+p)/2} \left| \mathbf{B}' \times \hat{\mathbf{n}}' \right|^{(p+1)/2} \tag{9}$$

$$Q = \kappa_p \int dV K_e \mathcal{D}^{(3+p)/2} \left| \mathbf{B}' \times \hat{\mathbf{n}}' \right|^{(p+1)/2} \cos 2\chi \tag{10}$$

$$U = \kappa_p \int dV K_e \mathcal{D}^{(3+p)/2} \left| \mathbf{B}' \times \hat{\mathbf{n}}' \right|^{(p+1)/2} \sin 2\chi, \tag{11}$$

where $\mathcal{D}$ is the Doppler factor, $\left| \mathbf{B}' \times \hat{\mathbf{n}}' \right|$ is the strength of the magnetic field component perpendicular to the line of sight, and χ is the angle between the polarization vector from a volume element and some reference direction in the plane of the sky that will be specified below. Primed quantities refer to the proper frame of the fluid. The integration volume is[2] $dV = R\,dR\,d\phi$, where $0 < \phi < 2\pi$ and $0 < R < R_0$. We also defined

$$\kappa_p = \frac{C_p \, \nu^{-(p-1)/2}}{D^2 (1+z)^{(3+p)/2}} \tag{12}$$

$$C_p = \frac{\sqrt{3}}{4} \Gamma_E \left(\frac{3p-1}{12} \right) \Gamma_E \left(\frac{3p+7}{12} \right) \frac{e^3}{m_e} \left(\frac{3e}{2\pi m_e^3} \right)^{(p-1)/2}, \tag{13}$$

where e and m_e are the charge and mass of the electron, ν is the observed radiation frequency, z is the cosmological redshift, D is the luminosity distance to the source, and Γ_E is the Euler gamma function. The degree of linear polarization is

$$\Pi = \frac{\sqrt{Q^2 + U^2}}{I}, \tag{14}$$

and the EVPA, Ψ, of the synchrotron radiation from the entire emission region (assumed to be unresolved) is given by

$$\cos 2\Psi = \frac{Q}{\sqrt{Q^2 + U^2}}, \qquad \sin 2\Psi = \frac{U}{\sqrt{Q^2 + U^2}}, \tag{15}$$

---

[1] Since we are dealing with ultra-relativistic particles, we neglected circular polarization and set $V = 0$.
[2] The Stokes parameters per unit jet length provide good estimates of Π and EVPA when the emission region is not very extended. For example, taking $dV = R\,dR\,d\phi\,dz$, where $z_0 - \Delta z < z < z_0$, we find that Π and EVPA change by <20% for $\Delta z/z_0 < 0.5$. Our results do not depend on the exact location of the emission region (i.e., fixing $\Gamma(R_0) = 10$ one finds that Π and EVPA are independent of z_0).

where $0 < \Psi < \pi$.

Now we express the quantities that appear in Eqs. (9)–(11) as a function of the electromagnetic fields in the observer's frame (our final expressions are given by Eqs. 21–23 below). We closely followed the framework developed by Del Zanna et al. (2006). The viewing angle θ_{obs} is measured with respect to the direction of the jet axis, $\hat{\mathbf{z}}$. Then, the unit vector directed toward the observer is $\hat{\mathbf{n}} = \sin\theta_{obs}\cos\phi\,\hat{\mathbf{R}} - \sin\theta_{obs}\sin\phi\,\hat{\boldsymbol{\phi}} + \cos\theta_{obs}\hat{\mathbf{z}}$. The polarization vector of the radiation from a volume element is (Lyutikov et al. 2003; Del Zanna et al. 2006)

$$\hat{\mathbf{e}} = \frac{\hat{\mathbf{n}} \times \mathbf{q}}{\sqrt{q^2 - (\mathbf{q} \cdot \hat{\mathbf{n}})^2}}, \qquad \mathbf{q} = \mathbf{B} - \hat{\mathbf{n}} \times \mathbf{E}. \tag{16}$$

We took as a reference direction the projection of the jet axis on the plane of the sky, which is $\hat{\mathbf{l}} = [(\hat{\mathbf{z}} \cdot \hat{\mathbf{n}})\hat{\mathbf{n}} - \hat{\mathbf{z}}]/\sqrt{1 - (\hat{\mathbf{z}} \cdot \hat{\mathbf{n}})^2}$ (note that $\hat{\mathbf{l}}$ is the unit vector orthogonal to $\hat{\mathbf{n}}$, and coplanar to $\hat{\mathbf{n}}$ and $\hat{\mathbf{z}}$). Then, one has $\cos\chi = \hat{\mathbf{e}} \cdot \hat{\mathbf{l}}$, and $\sin\chi = \hat{\mathbf{e}} \cdot (\hat{\mathbf{l}} \times \hat{\mathbf{n}})$, or equivalently

$$\cos\chi = \frac{\mathbf{q} \cdot (\hat{\mathbf{l}} \times \hat{\mathbf{n}})}{\sqrt{q^2 - (\mathbf{q} \cdot \hat{\mathbf{n}})^2}}, \qquad \sin\chi = -\frac{\mathbf{q} \cdot \hat{\mathbf{l}}}{\sqrt{q^2 - (\mathbf{q} \cdot \hat{\mathbf{n}})^2}}. \tag{17}$$

Since $\hat{\mathbf{l}} \times \hat{\mathbf{n}}$, $\hat{\mathbf{l}}$, $\hat{\mathbf{n}}$ are mutually orthogonal, any vector $\mathbf{X}$ can be conveniently decomposed as $\mathbf{X} = X_1 \hat{\mathbf{l}} \times \hat{\mathbf{n}} + X_2 \hat{\mathbf{l}} + X_3 \hat{\mathbf{n}}$, where $X_1 = \mathbf{X} \cdot (\hat{\mathbf{l}} \times \hat{\mathbf{n}})$, $X_2 = \mathbf{X} \cdot \hat{\mathbf{l}}$, $X_3 = \mathbf{X} \cdot \hat{\mathbf{n}}$. Below we need the first and second components of $\mathbf{q} = \mathbf{B} - \hat{\mathbf{n}} \times \mathbf{E}$, which are

$$q_1 = \left(E_R \cos\theta_{obs} - B_\phi \right) \cos\phi - E_z \sin\theta_{obs} - B_R \sin\phi \tag{18}$$

$$q_2 = \left(E_R - B_\phi \cos\theta_{obs} \right) \sin\phi - B_z \sin\theta_{obs} + B_R \cos\theta_{obs} \cos\phi, \tag{19}$$

and the third component of $\mathbf{v} = \mathbf{E} \times \mathbf{B}/B^2$, which is

$$v_3 = \frac{\left[(B_z E_R - B_R E_z) \sin\phi - B_\phi E_z \cos\phi \right] \sin\theta_{obs} + B_\phi E_R \cos\theta_{obs}}{B^2}. \tag{20}$$

Equation (17) gives $\cos\chi = q_1/\sqrt{q_1^2 + q_2^2}$ and $\sin\chi = -q_2/\sqrt{q_1^2 + q_2^2}$. Then one has

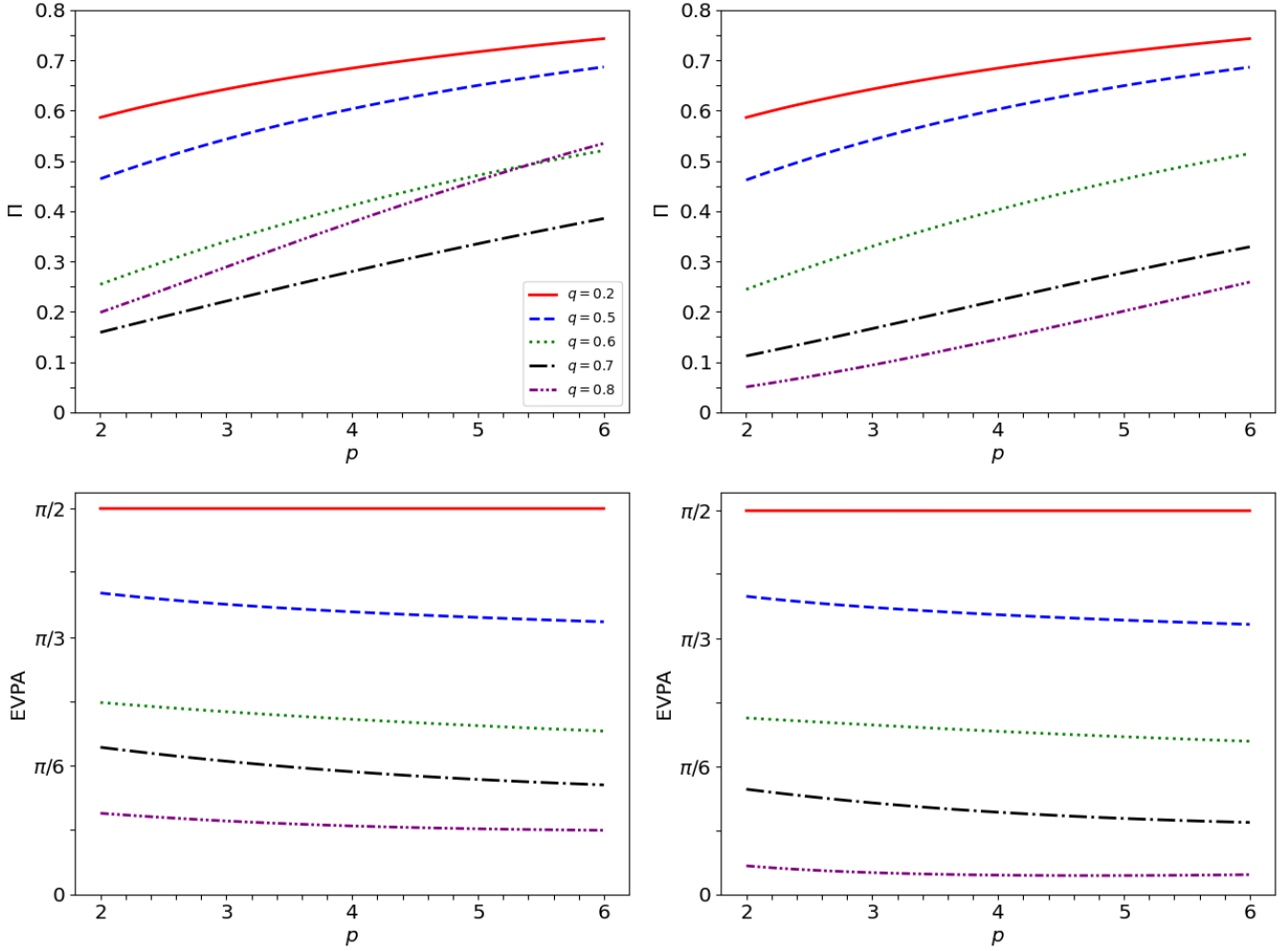$$\cos 2\chi = \frac{q_1^2 - q_2^2}{q_1^2 + q_2^2}, \qquad \sin 2\chi = -\frac{2q_1 q_2}{q_1^2 + q_2^2}. \tag{21}$$

Fig. 3. Polarization degree, Π (top panels) and EVPA (bottom panels) as a function of the power-law index, p, of the electron energy distribution. When EVPA = 0 and EVPA = $\pi/2$, the EVPA is respectively parallel and perpendicular to the projection of the jet axis on the plane of the sky. In the left panels the proper number density is assumed to be constant, whereas in the right panels the magnetization is assumed to be constant. The viewing angle is assumed to be $\theta_{\rm obs} = 0.1$ rad.

The Doppler factor, $\mathcal{D} = [\Gamma(1 - \mathbf{v} \cdot \hat{\mathbf{n}})]^{-1}$, can be presented as

$$\mathcal{D} = \frac{1}{\Gamma(1 - v_3)} \cdot \tag{22}$$

Taking into account that $\mathbf{v} \cdot \mathbf{B} = 0$, the strength of the magnetic field component perpendicular to the line of sight is (Del Zanna et al. 2006): $|\mathbf{B}' \times \hat{\mathbf{n}}'| = \Gamma^{-1} \sqrt{B^2 - \mathcal{D}^2(\mathbf{B} \cdot \hat{\mathbf{n}})^2}$. As we demonstrate in Appendix D, this expression is equivalent to

$$\left|\mathbf{B}' \times \hat{\mathbf{n}}'\right| = \mathcal{D}\sqrt{q_1^2 + q_2^2} \, . \tag{23}$$

To calculate the Stokes parameters, one needs to specify the electron number density K_e. We considered two different scenarios: a constant number density, $K_e = K_0$ (Sect. 3.1) and a constant magnetization, $K_e \propto B'^2$, where $B' = B/\Gamma$ is the magnetic field strength in the proper frame (Sect. 3.2). We assumed that the viewing angle is $\theta_{\rm obs} = 1/\Gamma(R_0) = 0.1$ rad. The effect of changing the viewing angle is discussed in Appendix A.

3.1. Constant number density

In the left panels of Fig. 3 we show the polarization degree Π and the EVPA obtained for a constant proper number density

(i.e., $K_e = K_0$) as a function of the power-law index, p, of the electron energy distribution. The spectrum of the emitted radiation is $F_\nu \propto \nu^{-\alpha}$, where $\alpha = (p - 1)/2$. The typical value of the optical spectral index of HSP blazars is $\alpha \sim 0.5$ (Fossati et al. 1998; Abdo et al. 2011; Ghisellini et al. 2017), which is obtained for $p = 2$. The X-ray spectral index is typically within the range $\alpha \sim 1.5$–2.5, which is obtained for $p = 4$–6. Hereafter, we assume the optical and X-ray polarization to be respectively $\Pi_{\rm O} = \Pi_{p=2}$ and $\Pi_{p=4} < \Pi_{\rm X} < \Pi_{p=6}$.

For small values of q, the polarization degree is close to the maximal one, which is $\Pi_{\rm max} = (p + 1)/(p + 7/3)$. For example, considering a jet with $q = 0.2$ we find[3] $\Pi_{\rm X} = 0.68$–0.74 and $\Pi_{\rm O} = 0.58$, whereas $\Pi_{\rm max,X} = 0.79$–0.84 and $\Pi_{\rm max,O} = 0.69$. The polarization degree is weakly chromatic, as $\Pi_{\rm X}/\Pi_{\rm O} = 1.2$. Considering $q = 0.05$–0.1, the polarization degree changes by less than a few percent with respect to the model with $q = 0.2$. The EVPA is nearly perpendicular to the projection of the jet axis on the plane of the sky, as expected since in the proper frame the magnetic field is predominantly poloidal (see Fig. 2).

---

[3] The X-ray polarization degree depends on the power-law index of the electron energy distribution. $\Pi_{\rm X} = 0.68$ and $\Pi_{\rm X} = 0.74$ are obtained for $p = 4$ and $p = 6$, respectively.

For large values of q, the polarization degree is much smaller than Π_{max}. For $q = 0.6$ we find $\Pi_X = 0.41$–0.52 and $\Pi_O = 0.25$, and for $q = 0.8$ we find $\Pi_X = 0.38$–0.54 and $\Pi_O = 0.20$. The polarization degree is strongly chromatic, as $\Pi_X/\Pi_O = 1.6$–2.7. This effect is entirely due to the softening of the electron energy distribution at high energies (we assumed $p = 2$ for the optical emitting electrons, and $p = 4$–6 for the X-ray emitting electrons). The chromaticity is much stronger than for a uniform magnetic field, where the polarization degree is $\Pi_{max} = (p + 1)/(p + 7/3)$ (Fig. 5 of Lyutikov et al. 2003 shows that the polarization degree can increase with p more rapidly than Π_{max}, consistent with our results). The EVPA is nearly parallel to the projection of the jet axis on the plane of the sky, as expected since in the proper frame the magnetic field is predominantly toroidal. For $q \gtrsim 0.8$ the polarization degree slightly increases, whereas the EVPA shows a continuous transition to EVPA = 0. As we discuss in Appendix B, an abrupt transition from EVPA $= \pi/2$ to EVPA = 0 is possible only for some special jet shapes.

3.2. Constant magnetization

In the right panels of Fig. 3 we show the polarization degree Π and the EVPA obtained for a constant magnetization (i.e., $K_e \propto B'^2 = B^2/\Gamma^2$). For small values of q, one has $B_\phi^2 - E^2 \ll B_p^2$ (see Fig. 2), and therefore $B'^2 = B^2 - E^2 \sim B_p^2$. Since B_p is independent of R, the polarization degree and the EVPA are similar to the scenario with constant number density.

For large values of q, one has $B_\phi^2 - E^2 \gg B_p^2$, and therefore $B'^2 \sim B_\phi^2 - E^2$. Since $B_\phi^2 - E^2 \propto R^4$ (see Eq. 6), the proper number density has a sharp peak near the jet boundary. The polarization degree is smaller with respect to the scenario with a constant number density. For $q = 0.6$ we find $\Pi_X = 0.40$–0.51 and $\Pi_O = 0.24$, and for $q = 0.8$ we find $\Pi_X = 0.15$–0.26 and $\Pi_O = 0.05$. Larger values of q would give a lower polarization degree. For example, for $q = 0.9$ we find $\Pi_X = 0.067$–0.15 and $\Pi_O = 0.016$. In this case, the chromaticity is very strong, as $\Pi_X/\Pi_O = 4.2$–9.3. However, the peak bulk Lorentz factor would be very large.

4. Discussion

We studied the polarization of the synchrotron radiation from HSP blazars. We used the axisymmetric stationary model of Lyubarsky (2009) to calculate the jet electromagnetic fields, as appropriate for blazars in a quiescent state. In this model, the transverse size of the jet can be parameterized as $R_0 \propto z_0^q$, where z_0 is the distance from the black hole. We considered two simple scenarios to populate the jet with nonthermal electrons (we assumed that either the magnetization or the electron proper number density across the jet is constant). The shape of the jet has a dramatic impact on the polarization:

- For $q \sim 0.2$ (a nearly cylindrical jet), the polarization degree is large and weakly chromatic (the X-ray and optical polarization degrees are respectively $\Pi_X \sim 70\%$ and $\Pi_O \sim 60\%$). The EVPA is nearly perpendicular to the projection of the jet axis on the plane of the sky.
- For $q \sim 0.6$–0.8 (a nearly parabolic jet), the polarization degree is lower and becomes strongly chromatic. We find $\Pi_X \sim 15$–50% and $\Pi_O \sim 5$–25% (the ratio is typically $\Pi_X/\Pi_O \sim 2$–5; however, the ratio can reach $\Pi_X/\Pi_O \sim 9$ for $q = 0.9$). The EVPA is nearly parallel to the projection of the jet axis on the plane of the sky.

We emphasize that in our model the optical and X-ray emitting electrons are co-spatial and only differ in terms of the power-law index of their energy distributions. The chromaticity is due to the softening of the electron distribution at high energies and is much stronger than for a uniform magnetic field. The polarization degree and the EVPA are determined by the global structure of the electromagnetic fields within the jet (the effect of a random component of the fields is discussed below).

Our results are important for interpreting multifrequency polarimetric observations of HSP blazars (Liodakis et al. 2022; Di Gesu et al. 2022; Ehlert et al. 2023; Errando et al. 2024; Kim et al. 2024). The observed X-ray polarization degree is $\Pi_X \sim 10$–20%, whereas the optical polarization degree is significantly smaller ($\Pi_X/\Pi_O \sim 2$–7). The EVPA seems to align with the projection of the jet axis on the plane of the sky[4]. Our results show that the jet should be nearly parabolic ($q \sim 0.6$–0.8), consistent with very long baseline interferometry observations of AGN jets on larger spatial scales (Mertens et al. 2016; Pushkarev et al. 2017; Kovalev et al. 2020; Boccardi et al. 2021).

Current multifrequency polarimetric observations of HSP blazars can hardly constrain the particle acceleration process. In our model the jet is Poynting-dominated, and therefore nonthermal particle acceleration is likely powered by magnetic reconnection rather than shocks (Sironi et al. 2015). The most energetic electrons trace the distribution of the reconnecting current sheets, as their cooling time is short. The Kelvin-Helmholtz instability at the interface between the jet and the external medium can produce current sheets near the jet boundary (Sironi et al. 2021). Instead, the kink instability can produce a more uniform distribution of current sheets across the jet (Alves et al. 2018; Davelaar et al. 2020). In the scenarios that we explored, the polarization degree and the EVPA are not very sensitive to the radial distribution of the electrons. As such, it is difficult to say whether reconnection is triggered by the Kelvin-Helmholtz or the kink instability.

We conclude by discussing some directions for future research:

(i) The electromagnetic fields may have a random component that changes on small spatial scales. If the random component is isotropic in the proper frame, and its strength is comparable to the regular component, the polarization degree decreases by a factor of ~ 2, whereas the EVPA does not change (Granot & Königl 2003; Bandiera & Petruk 2016). A time-dependent random magnetic field can produce fluctuations of the polarization degree and EVPA (Marscher 2014).

(ii) Nonthermal electrons could be continuously accelerated at a certain distance from the black hole and then advected along the jet for a cooling length. Since the cooling length depends on the electron energy, this leads to "energy stratification," as previously discussed for the shock acceleration scenario (Tavecchio et al. 2018, 2020). We emphasize that some energy stratification is expected in any conceivable scenario, as particles with a longer cooling time are advected farther away along the jet. The polarization degree is expected to decrease as the emission region becomes more spatially extended. This effect is chromatic (Π_O decreases more than Π_X because the corresponding electron cooling time is longer by a factor of $\sqrt{\nu_X/\nu_O} \sim 100$).

(iii) Both optical and X-ray EVPA swings have now been observed (Marscher et al. 2008, 2010; Abdo et al.

---

[4] The situation is far from clear, especially for the blazars 1ES 0229+200 (Ehlert et al. 2023) and Mrk 421 (Di Gesu et al. 2022). As noted in Di Gesu et al. (2022), the jet could bend by tens of degrees between the inner region (where the X-ray and optical emission are likely produced) and the outer region imaged in the radio band.

2010; Larionov et al. 2013; Blinov et al. 2015, 2016, 2018; Kiehlmann et al. 2016; Di Gesu et al. 2023; Middei et al. 2023b). To explain the EVPA swings, one should abandon the axisymmetric stationary jet model that we used throughout this paper. The fact that optical and X-ray EVPA swings are not simultaneous suggests that, due to energy stratification, the emitting electrons are not exactly co-spatial (Di Gesu et al. 2023; Middei et al. 2023b).

References

Abdo, A. A., Ackermann, M., Ajello, M., et al. 2010, Nature, 463, 919
Abdo, A. A., Ackermann, M., Ajello, M., et al. 2011, ApJ, 736, 131
Alves, E. P., Zrake, J., & Fiuza, F. 2018, Phys. Rev. Lett., 121, 245101
Bandiera, R., & Petruk, O. 2016, MNRAS, 459, 178
Blandford, R. D., & Königl, A. 1979, ApJ, 232, 34
Blandford, R. D., & Payne, D. G. 1982, MNRAS, 199, 883
Blandford, R. D., & Znajek, R. L. 1977, MNRAS, 179, 433
Blandford, R., Meier, D., & Readhead, A. 2019, ARA&A, 57, 467
Blinov, D., Pavlidou, V., Papadakis, I., et al. 2015, MNRAS, 453, 1669
Blinov, D., Pavlidou, V., Papadakis, I. E., et al. 2016, MNRAS, 457, 2252
Blinov, D., Pavlidou, V., Papadakis, I., et al. 2018, MNRAS, 474, 1296
Boccardi, B., Perucho, M., Casadio, C., et al. 2021, A&A, 647, A67
Böttcher, M. 2019, Galaxies, 7, 20
Davelaar, J., Philippov, A. A., Bromberg, O., & Singh, C. B. 2020, ApJ, 896, L31
Del Zanna, L., Volpi, D., Amato, E., & Bucciantini, N. 2006, A&A, 453, 621
Di Gesu, L., Donnarumma, I., Tavecchio, F., et al. 2022, ApJ, 938, L7
Di Gesu, L., Marshall, H. L., Ehlert, S. R., et al. 2023, Nat. Astron., 7, 1245
Ehlert, S. R., Liodakis, I., Middei, R., et al. 2023, ApJ, 959, 61
Errando, M., Liodakis, I., Marscher, A. P., et al. 2024, ApJ, 963, 5
Fossati, G., Maraschi, L., Celotti, A., Comastri, A., & Ghisellini, G. 1998, MNRAS, 299, 433

Ghisellini, G., Righi, C., Costamante, L., & Tavecchio, F. 2017, MNRAS, 469, 255
Granot, J., & Königl, A. 2003, ApJ, 594, L83
Kiehlmann, S., Savolainen, T., Jorstad, S. G., et al. 2016, A&A, 590, A10
Kim, D. E., Di Gesu, L., Liodakis, I., et al. 2024, A&A, 681, A12
Komissarov, S. S., Barkov, M. V., Vlahakis, N., & Königl, A. 2007, MNRAS, 380, 51
Komissarov, S. S., Vlahakis, N., Königl, A., & Barkov, M. V. 2009, MNRAS, 394, 1182
Kovalev, Y. Y., Pushkarev, A. B., Nokhrina, E. E., et al. 2020, MNRAS, 495, 3576
Larionov, V. M., Jorstad, S. G., Marscher, A. P., et al. 2013, ApJ, 768, 40
Liodakis, I., Marscher, A. P., Agudo, I., et al. 2022, Nature, 611, 677
Lyubarsky, Y. 2009, ApJ, 698, 1570
Lyubarsky, Y. 2010, MNRAS, 402, 353
Lyubarsky, Y., et al. 2011, Phys. Rev. E, 83, 016302
Lyutikov, M., Pariev, V. I., & Blandford, R. D. 2003, ApJ, 597, 998
Lyutikov, M., Pariev, V. I., & Gabuzda, D. C. 2005, MNRAS, 360, 869
Marscher, A. P. 2014, ApJ, 780, 87
Marscher, A. P., & Jorstad, S. G. 2021, Galaxies, 9, 27
Marscher, A. P., Jorstad, S. G., D'Arcangelo, F. D., et al. 2008, Nature, 452, 966
Marscher, A. P., Jorstad, S. G., Larionov, V. M., et al. 2010, ApJ, 710, L126
Marshall, H. L., Liodakis, I., & Marscher, A. P. 2023, ArXiv e-prints [arXiv:2310.11510]
Mertens, F., Lobanov, A. P., Walker, R. C., & Hardee, P. E. 2016, A&A, 595, A54
Middei, R., Liodakis, I., Perri, M., et al. 2023a, ApJ, 942, L10
Middei, R., Perri, M., Puccetti, S., et al. 2023b, ApJ, 953, L28
Pariev, V. I., Istomin, Y. N., & Beresnyak, A. R. 2003, A&A, 403, 805
Peirson, A. L., Negro, M., Liodakis, I., et al. 2023, ApJ, 948, L25
Pushkarev, A. B., Kovalev, Y. Y., Lister, M. L., & Savolainen, T. 2017, MNRAS, 468, 4992
Romero, G. E., Boettcher, M., Markoff, S., & Tavecchio, F. 2017, Space Sci. Rev., 207, 5
Sironi, L., Petropoulou, M., & Giannios, D. 2015, MNRAS, 450, 183
Sironi, L., Rowan, M. E., & Narayan, R. 2021, ApJ, 907, L44
Tavecchio, F. 2021, Galaxies, 9, 37
Tavecchio, F., Landoni, M., Sironi, L., & Coppi, P. 2018, MNRAS, 480, 2872
Tavecchio, F., Landoni, M., Sironi, L., & Coppi, P. 2020, MNRAS, 498, 599
Tchekhovskoy, A., McKinney, J. C., & Narayan, R. 2008, MNRAS, 388, 551
Tchekhovskoy, A., McKinney, J. C., & Narayan, R. 2009, ApJ, 699, 1789
Tchekhovskoy, A., Narayan, R., & McKinney, J. C. 2011, MNRAS, 418, L79
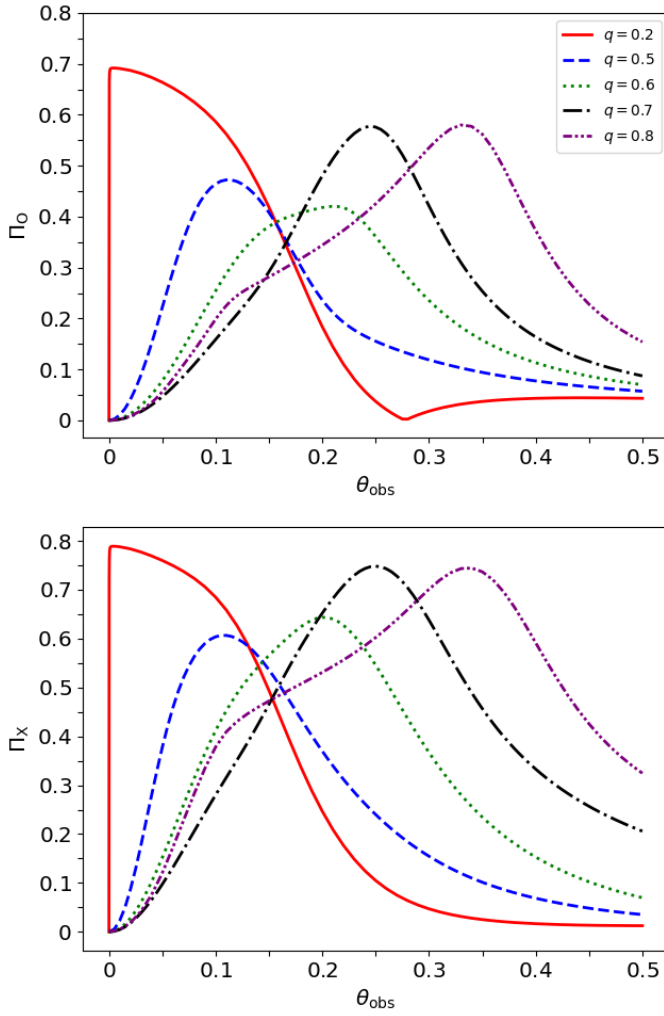Vlahakis, N. 2004, ApJ, 600, 324

Fig. A.1. Optical polarization degree, $\Pi_O = \Pi_{p=2}$ (top panel) and X-ray polarization degree, $\Pi_X = \Pi_{p=4}$ (bottom panel) as a function of the viewing angle, θ_{obs}, which is expressed in radians. The proper number density of the emitting electrons is assumed to be constant.

Appendix A: Effect of the viewing angle

We investigated the dependence of the polarization degree on the viewing angle. We assumed that the proper number density of the emitting electrons is constant. In the top panel of Fig. A.1 we show the optical polarization degree, and in the bottom panel we show the X-ray polarization degree. Both Π_O and Π_X show a similar dependence on θ_{obs}. The most important difference is that Π_O is smaller than Π_X for a given θ_{obs}.

The polarization degree vanishes for $\theta_{obs} = 0$, as expected from symmetry considerations. For $q \sim 0.2$, the polarization degree rises almost abruptly to Π_{max}, and then decreases for large θ_{obs}. For $q \sim 0.5 - 0.8$, the rise is more gradual, and the peak polarization is smaller than Π_{max}.

Appendix B: Special jet shapes

In the general case discussed in Sect. 3, the Stokes parameter U does not vanish. However, for the special jet shapes discussed below one finds $U = 0$. When $U = 0$, the EVPA can be either parallel or perpendicular to the projection of the jet axis on the plane of the sky.

Lyutikov et al. (2003) considered a conical jet with $B_R = B_z = 0$. In this case, one has

$$q_1 = \left(E_R \cos\theta_{obs} - B_\phi\right)\cos\phi - E_z \sin\theta_{obs} \tag{B.1}$$

$$q_2 = \left(E_R - B_\phi \cos\theta_{obs}\right)\sin\phi \tag{B.2}$$

$$v_3 = \frac{B_\phi E_R \cos\theta_{obs} - B_\phi E_z \cos\phi \sin\theta_{obs}}{B^2} . \tag{B.3}$$

For a given viewing angle θ_{obs}, the Doppler factor is a function of R and $\cos\phi$:

$$\mathcal{D} = \frac{1}{\Gamma\left(1 - v_3\right)} = f_1\left(R, \cos\phi\right) . \tag{B.4}$$

Since $q_1^2 + q_2^2$ is also a function of R and $\cos\phi$, one has

$$\left|\mathbf{B}' \times \hat{\mathbf{n}}'\right| = \mathcal{D}\sqrt{q_1^2 + q_2^2} = f_2\left(R, \cos\phi\right) . \tag{B.5}$$

Finally, one finds

$$\sin 2\chi = -\frac{2q_1 q_2}{q_1^2 + q_2^2} = f_3\left(R, \cos\phi\right)\sin\phi . \tag{B.6}$$

The functions f_1, f_2, f_3 are defined through Eqs. (B.4)-(B.6). Substituting Eqs. (B.4)-(B.6) into Eq. (11), one finds

$$U = \int_0^{R_0} R dR \int_0^{2\pi} d\phi \; F(R, \cos\phi)\sin\phi , \tag{B.7}$$

where the function F can be expressed as a combination of f_1, f_2, f_3. It is clear that $U = 0$ for any function F.

Pariev et al. (2003) and Lyutikov et al. (2005) considered a cylindrical jet with $E_z = B_R = 0$. In this case, one has

$$q_1 = \left(E_R \cos\theta_{obs} - B_\phi\right)\cos\phi \tag{B.8}$$

$$q_2 = \left(E_R - B_\phi \cos\theta_{obs}\right)\sin\phi - B_z \sin\theta_{obs} \tag{B.9}$$

$$v_3 = \frac{B_\phi E_R \cos\theta_{obs} + B_z E_R \sin\phi \sin\theta_{obs}}{B^2} . \tag{B.10}$$

The Doppler factor is a function of R and $\sin\phi$:

$$\mathcal{D} = \frac{1}{\Gamma\left(1 - v_3\right)} = g_1\left(R, \sin\phi\right) . \tag{B.11}$$

Since $q_1^2 + q_2^2$ is also a function of R and $\sin\phi$, one has

$$\left|\mathbf{B}' \times \hat{\mathbf{n}}'\right| = \mathcal{D}\sqrt{q_1^2 + q_2^2} = g_2\left(R, \sin\phi\right) . \tag{B.12}$$

Finally, one finds

$$\sin 2\chi = -\frac{2q_1 q_2}{q_1^2 + q_2^2} = g_3\left(R, \sin\phi\right)\cos\phi . \tag{B.13}$$

Substituting Eqs. (B.11)-(B.13) into Eq. (11), one finds

$$U = \int_0^{R_0} R dR \int_0^{2\pi} d\phi \; G(R, \sin\phi)\cos\phi , \tag{B.14}$$

which gives $U = 0$.

Appendix C: Details of the jet structure

When the jet is accelerated to bulk Lorentz factors $\Gamma \gg 1$, Eq. (29) of Lyubarsky (2009) gives

$$\frac{B_\phi^2 - E^2}{B_p^2} = \frac{\Omega^2 R^2}{\Gamma^2} - 1 \ . \tag{C.1}$$

Following Lyubarsky (2009), we defined $X = \Omega R$ and $Z = \Omega z_0$. The shape of the flux surfaces was determined by their Eq. (74), which gives $\psi/\psi_0 = X^2/\sqrt{3}Y^2$, where $Y = CZ^q$. Substituting this expression into their Eq. (75), one finds

$$\frac{\Omega^2 R^2}{\Gamma^2} - 1 = \frac{q(1-q)}{3}\frac{X^4}{Z^2} \ . \tag{C.2}$$

Since the background magnetic field is assumed to be uniform, one has $\psi/\psi_0 = R^2/R_0^2 = X^2/\Omega^2 R_0^2$. As discussed above, one has also $\psi/\psi_0 = X^2/\sqrt{3}C^2 Z^{2q}$. Then, one finds

$$Z^2 = \left(\frac{\Omega R_0}{3^{1/4}C}\right)^{2/q} \ . \tag{C.3}$$

Eq. (6) immediately follows from Eqs. (C.1)-(C.3).

Appendix D: Perpendicular magnetic field

We calculated the strength of the magnetic field component perpendicular to the line of sight. First of all, we demonstrated two useful identities. The first identity is

$$[(\mathbf{E} \times \mathbf{B}) \cdot \hat{\mathbf{n}}]^2 = E^2 B^2 - (\mathbf{B} \cdot \hat{\mathbf{n}})^2 E^2 - (\mathbf{E} \cdot \hat{\mathbf{n}})^2 B^2 \ , \tag{D.1}$$

which can be demonstrated as follows. Consider the vector $\mathbf{P} = (\mathbf{E} \times \mathbf{B}) \times \hat{\mathbf{n}}$. One has

$$P^2 = (\mathbf{E} \times \mathbf{B})^2 - [(\mathbf{E} \times \mathbf{B}) \cdot \hat{\mathbf{n}}]^2 = E^2 B^2 - [(\mathbf{E} \times \mathbf{B}) \cdot \hat{\mathbf{n}}]^2 \ , \tag{D.2}$$

where we used the fact that $\mathbf{E} \cdot \mathbf{B} = 0$. Since $\mathbf{P} = (\mathbf{E} \cdot \hat{\mathbf{n}})\mathbf{B} - (\mathbf{B} \cdot \hat{\mathbf{n}})\mathbf{E}$, one also has

$$P^2 = (\mathbf{B} \cdot \hat{\mathbf{n}})^2 E^2 + (\mathbf{E} \cdot \hat{\mathbf{n}})^2 B^2 \ . \tag{D.3}$$

Equation (D.1) immediately follows from Eqs. (D.2)-(D.3). The second identity, which is obtained using the first one, is

$$\frac{1}{\Gamma^2 \mathcal{D}^2} = \left[1 - \frac{(\mathbf{E} \times \mathbf{B}) \cdot \hat{\mathbf{n}}}{B^2}\right]^2 =$$
$$= 1 - \frac{2(\mathbf{E} \times \mathbf{B}) \cdot \hat{\mathbf{n}}}{B^2} + \frac{E^2}{B^2} - \frac{(\mathbf{B} \cdot \hat{\mathbf{n}})^2 E^2}{B^4} - \frac{(\mathbf{E} \cdot \hat{\mathbf{n}})^2}{B^2}. \tag{D.4}$$

The strength of the magnetic field component perpendicular to the line of sight is $|\mathbf{B}' \times \hat{\mathbf{n}}'| = \Gamma^{-1}\sqrt{B^2 - \mathcal{D}^2(\mathbf{B} \cdot \hat{\mathbf{n}})^2}$. This equation can be presented as

$$\left|\mathbf{B}' \times \hat{\mathbf{n}}'\right| = \mathcal{D}\sqrt{\frac{B^2}{\Gamma^2 \mathcal{D}^2} - \frac{(\mathbf{B} \cdot \hat{\mathbf{n}})^2}{\Gamma^2}} =$$
$$= \mathcal{D}\sqrt{\frac{B^2}{\Gamma^2 \mathcal{D}^2} - (\mathbf{B} \cdot \hat{\mathbf{n}})^2 + \frac{(\mathbf{B} \cdot \hat{\mathbf{n}})^2 E^2}{B^2}} =$$
$$= \mathcal{D}\sqrt{B^2 - (\mathbf{B} \cdot \hat{\mathbf{n}})^2 + E^2 - (\mathbf{E} \cdot \hat{\mathbf{n}})^2 - 2(\mathbf{E} \times \mathbf{B}) \cdot \hat{\mathbf{n}}} \ , \tag{D.5}$$

where we used Eq. (D.4) to obtain the final expression. Now consider the vector $\mathbf{q} = \mathbf{B} - \hat{\mathbf{n}} \times \mathbf{E}$. One has

$$q^2 = B^2 + E^2 - (\mathbf{E} \cdot \hat{\mathbf{n}})^2 - 2(\mathbf{E} \times \mathbf{B}) \cdot \hat{\mathbf{n}} \tag{D.6}$$
$$(\mathbf{q} \cdot \hat{\mathbf{n}})^2 = (\mathbf{B} \cdot \hat{\mathbf{n}})^2 \ . \tag{D.7}$$

From Eqs. (D.5)-(D.7), it follows that

$$\left|\mathbf{B}' \times \hat{\mathbf{n}}'\right| = \mathcal{D}\sqrt{q^2 - (\mathbf{q} \cdot \hat{\mathbf{n}})^2} \ , \tag{D.8}$$

which is equivalent to Eq. (23).